Computer Science Journal of Moldova, vol.**22**, no.2(65), 2014

Detection of Blood Vessels in Retinal Fundus Images*

Invited Article

Faraz Oloumi, Ashis K. Dhara,
Rangaraj M. Rangayyan[@], Sudipta Mukhopadhyay

Abstract

Detection of blood vessels in retinal fundus images is an important initial step in the development of systems for computer-aided diagnosis of pathologies of the eye. In this study, we perform multifeature analysis for the detection of blood vessels in retinal fundus images. The vessel detection techniques implemented include multiscale vesselness measures, Gabor filters, line operators, and matched filters. The selection of an appropriate threshold is crucial for accurate detection of retinal blood vessels. We evaluate an adaptive threshold selection method along with several others for this purpose. We also propose a postprocessing technique for removal of false-positive pixels around the optic nerve head. Values of the area under the receiver operating characteristic curve of up to 0.961 were obtained using the 20 test images of the DRIVE database.

Keywords: Gabor filter, line operator, matched filter, multiscale analysis, retinal fundus image, vessel detection, vesselness measure.

*This work was supported by grants from the Natural Sciences and Engineering Research Council (NSERC) of Canada, the Shastri Indo-Canadian Institute, and the Indian Institute of Technology Kharagpur, India. This article is a revised and expanded version of the conference publication cited as Dhara et al. [1]. @Address all correspondence to R. M. Rangayyan, ranga@ucalgary.ca

1 Introduction

Retinal fundus images are used by ophthalmologists for the diagnosis of several disorders, such as diabetic retinopathy (DR), retinopathy of prematurity, and maculopathy [2–4]. Detection of blood vessels is an important initial step in the development of computer-aided diagnostic (CAD) systems and analysis of retinal fundus images. It is possible to detect other anatomical landmarks such as the optic nerve head (ONH) and the macula in the retina with respect to the vascular architecture. The location and certain characteristics of such landmarks can help in the derivation of features for the detection of abnormalities. A variety of methods have been proposed for the detection of blood vessels; some of these methods are reviewed in the following paragraphs.

Chaudhuri et al. [5] proposed an algorithm based on two-dimensional (2D) matched filters for vessel detection. Their method is based on three assumptions: (i) the intensity profile of a vessel can be approximated by a Gaussian function, (ii) vessels can be approximated by piecewise linear segments, and (iii) the width of vessels is relatively constant. Detection of blood vessels was performed by convolving the given image with the matched filter rotated in several orientations. The maximum filter response over all orientations was assigned to each pixel.

Staal et al. [6] extracted the ridges in the images which roughly coincide with the vessel centerlines. In the next step, image primitives were obtained by grouping image ridges into sets that model straight-line elements, which were used to partition the image by assigning each pixel to the closest primitive set. Feature vectors were then computed for every pixel using the characteristics of the partitions and their line elements. The features were used for classification using a k-nearest-neighbor classifier. Staal et al. achieved an area under the receiver operating operating characteristic (ROC) curve of $A_z = 0.9520$ with 20 images of the test set of the DRIVE database [7].

Soares et al. [8] applied complex Gabor filters for feature extraction and supervised classification for the detection of blood vessels in retinal fundus images. In this method, the magnitude outputs at several scales

obtained from 2D complex Gabor filters were assigned to each pixel as a feature vector. Then, a Bayesian classifier was applied for classification of the results into vessel or nonvessel pixels. Soares et al. reported $A_z = 0.9614$ for the 20 test images of the DRIVE database.

Blood vessels can be considered as dark elongated curvilinear structures of different width and orientation on a brighter background. Several types of vesselness measures have been developed for the detection of blood vessels based on the properties of the eigenvalues of the Hessian matrix computed at each pixel. Because blood vessels are of varying width, different scales are used to calculate the eigenvalues and the maximum response at each pixel over all scales is used for further analysis. Frangi et al. [9] and Salem et al. [10] proposed different vesselness measures to highlight vessel-like structures. Wu et al. [11] applied the vesselness measure of Frangi et al. to the 40 training and testing images of the DRIVE database and reported $A_z = 0.9485$. Salem et al. [10] reported $A_z = 0.9450$ using 20 images of the STARE database [12].

Lupaşcu et al. [13] performed multifeature analysis using previously proposed features [6, 8, 9, 14, 17], combined with new features that represent information about the local intensity, the structure of vessels, spatial properties, and the geometry of the vessels at different scales of length. They used a feature vector containing a total of 41 features obtained at different scales to train a classifier, which was then applied to the test set. They reported $A_z = 0.9561$ using the 20 test images of the DRIVE database.

Rangayyan et al. [15] performed multiscale analysis for the detection of blood vessels using Gabor filters and classified pixels using multilayer perceptron (MLP) neural networks and reported A_z of 0.9597 with the test set of the DRIVE database. Oloumi [16] used multiscale Gabor filter magnitude responses, coherence, and the inverted green channel as features to train an MLP and achieved an A_z value of 0.9611 using the test set of the DRIVE database.

Other available methods in the literature that do not employ a filtering technique for the detection of the blood vessels include, but are not limited to, segmentation using multiconcavity modeling [18]; fractal analysis [19]; mathematical morphology and curvature evaluation [20];

and geometrical models and analysis of topological properties of the blood vessels [21].

In the present work, we perform vessel segmentation by multifeature analysis, using multiscale Gabor filters as proposed by Rangayyan et al. [15], multiscale vesselness measures as proposed by Frangi et al. [9] and Salem et al. [10], matched filters as proposed by Chaudhuri et al. [5], line operators [22], and a gamma-corrected version of the inverted green channel. Thresholding and binarization of the result of vessel detection is a crucial step for further analysis of the characteristics of blood vessels such as thickness and tortuosity [23]; we propose an adaptive thresholding technique by analyzing the intensity values of the boundary pixels of retinal blood vessels and compare the results against several automated thresholding methods. Most of the reported methods for the detection of blood vessels cause false-positive (FP) pixels associated with the boundary of the ONH. We propose a postprocessing technique for removal of FP pixels around the ONH.

2 Database of Retinal Images

In this work, retinal fundus images from the DRIVE database were used to assess the performance of the methods. The images of the DRIVE database [6, 7] were acquired during a screening program for DR in the Netherlands and show signs of mild DR. The images have a size 565×584 pixels and a field of view (FOV) of 45°. The DRIVE images are considered to be low-resolution retinal images; the images have an approximate spatial resolution of 20 μm per pixel. The DRIVE database consists of 40 images, which are labeled in two sets of 20 images for training and testing. A manually segmented image (ground-truth) of the vasculature is available for each image in the DRIVE database. Figure 1 shows the original color image 12 of the DRIVE database and its ground-truth image.

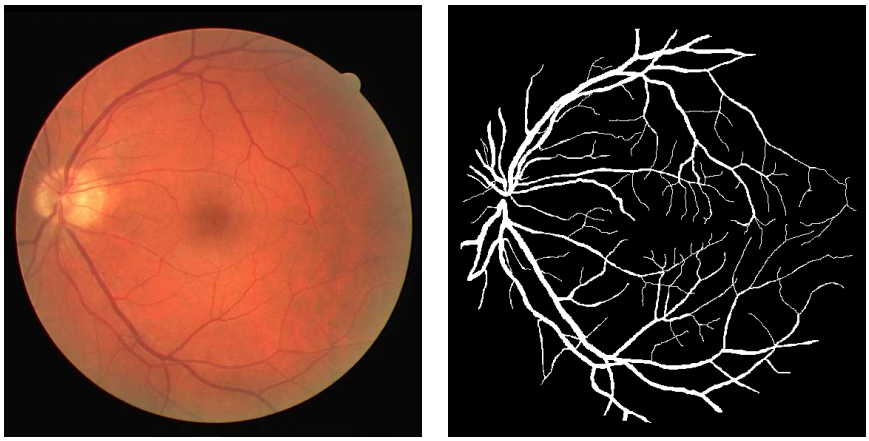

(a) (b)

Figure 1. (a) Original color image 12 of the DRIVE database. (b) Ground-truth of the image in part (a), as provided in the database.

3 Detection of Retinal Blood Vessels

In the present study, we review and implement several methods for the detection of blood vessels and investigate their combined application for multifeature analysis.

3.1 Vesselness Measures

Frangi et al. [9] defined a vesselness measure to detect pixels having vessel-like structures based on the properties of the eigenvalues of the Hessian matrix. A numerical estimate of the Hessian matrix, H, at each pixel of the given image, $L(x, y)$, is obtained as

$$H = \begin{bmatrix} \frac{\partial^2 L}{\partial x^2} & \frac{\partial^2 L}{\partial x \partial y} \\ \\ \frac{\partial^2 L}{\partial y \partial x} & \frac{\partial^2 L}{\partial y^2} \end{bmatrix}. \tag{1}$$

The entries of H can be obtained at multiple scales by convolving the

image $L(x, y)$ with the Gaussian kernel $G(x, y; \sigma)$ of different scales σ, defined as

$$G(x, y; \sigma) = \frac{1}{2\pi\sigma^2} \exp\left(-\frac{x^2 + y^2}{2\sigma^2}\right). \tag{2}$$

The width of retinal blood vessels varies from 50 μm to 200 μm in retinal fundus images, which translates to the range of about 2 to 10 pixels, given a spatial resolution of 20 μm for the DRIVE images. Gaussian kernels can be used to generate a suitable scale space with an amplitude range of σ related to the range of vessel width. Multiscale derivatives of the image $L(x, y)$ can be obtained by linear convolution of the image with the scale-normalized derivatives of the Gaussian kernel as $\frac{\partial^2 L}{\partial x^2} = L(x, y) * \sigma^2 G_{xx} = L_{xx}$, $\frac{\partial^2 L}{\partial x \partial y} = \frac{\partial^2 L}{\partial y \partial x} = L(x, y) * \sigma^2 G_{xy} = L_{xy} = L_{yx}$, and $\frac{\partial^2 L}{\partial y^2} = L(x, y) * \sigma^2 G_{yy} = L_{yy}$. Here G_{xx}, G_{xy}, and G_{yy} are the second derivatives of the Gaussian kernel G, and the symbol '$*$' represents the 2D convolution operation.

The Hessian matrix is symmetrical with real eigenvalues. The signs and ratios of the eigenvalues can be used as signatures of a local structure. Let λ_1 and λ_2 represent the eigenvalues of the Hessian matrix, with the condition $|\lambda_2| \geq |\lambda_1|$. The larger eigenvalue, λ_2, corresponds to the maximum principal curvature at the location (x, y). A larger value of λ_2 compared to λ_1 represents a vessel-like structure. The eigenvalues and eigenvectors of the Hessian matrix can be computed by solving the following equation:

$$\begin{vmatrix} L_{xx} - \lambda & L_{xy} \\ L_{yx} & L_{yy} - \lambda \end{vmatrix} = 0, \tag{3}$$

where λ represents the two eigenvalues λ_1 and λ_2. The eigenvalues λ_1 and λ_2 can be obtained as

$$\lambda_1 = \frac{L_{xx} + L_{yy} - \alpha}{2}, \tag{4}$$

and

$$\lambda_2 = \frac{L_{xx} + L_{yy} + \alpha}{2}, \tag{5}$$

where $\alpha = \sqrt{(L_{xx} - L_{yy})^2 + 4L_{xy}^2}$. Based on the property of the eigenvalues of the Hessian matrix, Frangi et al. [9] defined a vesselness measure to highlight pixels belonging to vessel-like structures as

$$V_F = \begin{cases} \exp\left(-\frac{R_\beta^2}{2\beta^2}\right)\left[1 - \exp\left(-\frac{S^2}{2\gamma^2}\right)\right] & \text{if } \lambda_1, \lambda_2 < 0, \\ 0 & \text{otherwise,} \end{cases} \tag{6}$$

where $R_\beta = \frac{\lambda_1}{\lambda_2}$, $S = \sqrt{{\lambda_1}^2 + {\lambda_2}^2}$ is the Frobenius norm of the Hessian matrix, $\beta = 0.5$ (as used by Frangi et al. [9]), and γ is equal to one-half of the maximum of all of the Frobenius norms computed for the whole image. The Frobenius norm is expected to be low in background areas where no vessels are present and the eigenvalues are low, because the magnitude of the derivatives of the intensities will be small. On the other hand, in regions with high contrast as compared to the background, the Frobenius norm will become larger, because at least one of the eigenvalues will be large.

The vesselness measure proposed by Salem et al. [10] uses the eigenvalues of the Hessian matrix to detect the orientation of blood vessels. Let $\vec{e}_1$ and $\vec{e}_2$ be the eigenvectors corresponding to the eigenvalues λ_1 and λ_2, respectively, and let θ_1 and θ_2 be the angles of the eigenvectors with respect to the positive x-axis. The orientations of the eigenvectors corresponding to the larger and smaller eigenvalues for every fifth pixel are shown in Figure 2. It can be noted from Figure 2 that the variation of the orientation of the eigenvectors corresponding to the smaller eigenvalues is smaller inside the blood vessels as compared to that outside the blood vessels. The eigenvectors corresponding to the smaller eigenvalues are mainly oriented along the blood vessels; hence, the angle θ_1 is used to analyze the orientation of blood vessels. The orientation of the eigenvector $\vec{e}_1$ can be represented as

$$\theta_1 = \arctan\left(-\frac{2L_{xy}}{L_{yy} - L_{xx} + \alpha}\right). \tag{7}$$

Detection of blood vessels can be accomplished by assuming that

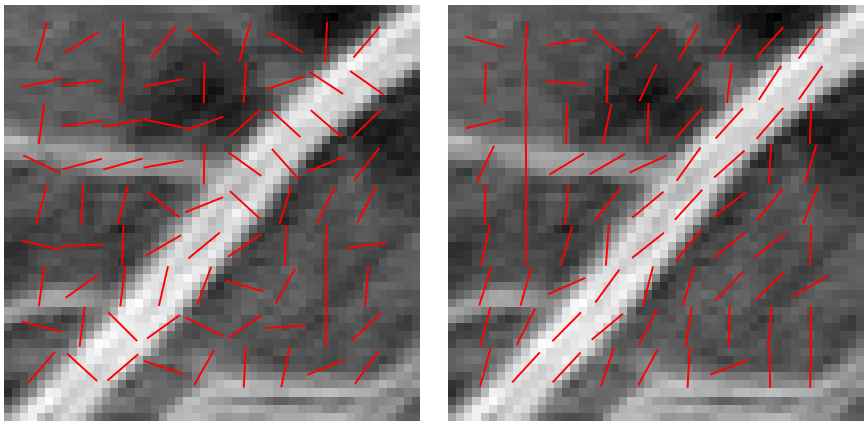

(a) (b)

Figure 2. Orientation of the eigenvectors corresponding to (a) the larger eigenvalue and (b) the smaller eigenvalue at each pixel for a part of a retinal fundus image with parts of blood vessels. Straight lines corresponding to the eigenvectors are shown for every fifth pixel. The size of the image is 50×50 pixels.

the maximum value of λ_2 ($\lambda_{\max}$) over several scales of σ is at the center of the vessel. Salem et al. [10] defined a vesselness measure as

$$V_S = \frac{\lambda_{\max}}{\theta_{\text{std}} + 1}, \tag{8}$$

where θ_{std} is the standard deviation (STD) of θ_1 over all scales used for the pixel under consideration. The larger the value of V_S for a pixel, the higher the probability that the pixel belongs to a vessel.

In this work, the range of scales $\sigma = [1, 6]$ with steps of 0.05 was determined to be the most suitable range for the vesselness measures of Frangi et al. and Salem et al. using the training set of the DRIVE database, and was used for subsequent analysis. Note that the two vesselness measures implemented in this work perform multiscale analysis by taking the maximum intensity value among all the available scales of σ. The implementation of the method of Frangi et al. used in this

work was provided by Dirk-Jan Kroon of University of Twente [36].

Figure 3 shows the magnitude response images of the result of applying the vesselness measures of Frangi et al. and Salem et al. to the image in Figure 1 (a).

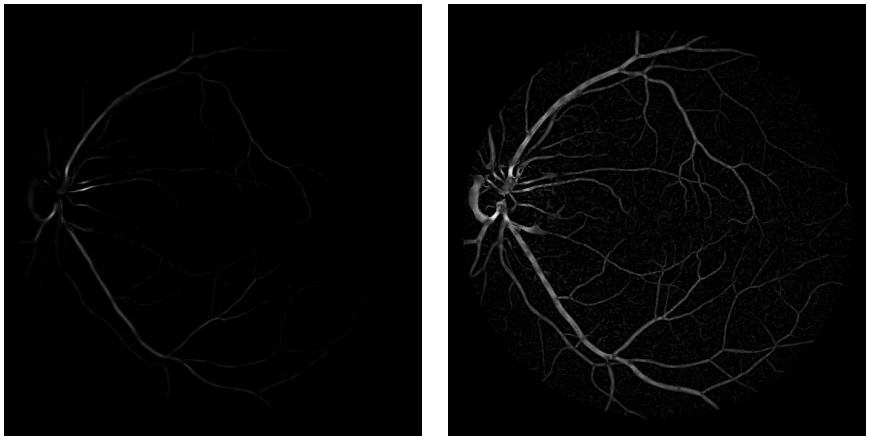

(a) (b)

Figure 3. Magnitude response images of the result of filtering the image in Figure 1 (a) obtained using (a) vesselness measure of Frangi et al. and (b) vesselness measure of Salem et al. Note that the result of the method of Frangi et al. provides lower intensity values as compared to the method of Salem et al. and the detected vessels may not be clearly visible in the result.

3.2 Gabor Filters

Rangayyan et al. [15] applied multiscale Gabor filters for the detection of blood vessels by considering the fact that blood vessels are elongated, piecewise-linear, or curvilinear structures with a preferred orientation. Gabor filters are sinusoidally modulated Gaussian functions that are suitable for the analysis of oriented structures because they provide optimal localization in both the frequency and space domains. The real Gabor filter kernel oriented at the angle $\theta = -\pi/2$ can be represented

as [15]

$$g(x,y) = \frac{1}{2\pi\sigma_x\sigma_y} \exp\left[-\frac{1}{2}\left(\frac{x^2}{\sigma_x^2} + \frac{y^2}{\sigma_y^2}\right)\right] \cos(2\pi f_o x)\,. \tag{9}$$

In this equation, the frequency of the modulating sinusoid is given by f_o, and σ_x and σ_y are the STD values in the x and y directions. For simplicity of design, a variable τ is used to represent the average thickness of the vessels to be detected. The value of σ_x is defined based on τ as $\sigma_x = \frac{\tau}{2\sqrt{2\ln 2}}$ and $\sigma_y = l\sigma_x$, where l represents the elongation of blood vessels. A bank of K Gabor filters may be obtained by rotating the main Gabor filter kernel given in Equation 9 over the range $[-\pi/2, \pi/2]$. For a given pixel, the maximum output value over all K filters is saved as the Gabor magnitude response at that particular pixel; the corresponding angle is saved as the Gabor angle response.

Values of $\tau = 8$ pixels, $l = 2.9$, and $K = 180$ were determined to provide the best single-scale results, as determined using the training set of the DRIVE database. Values of $\tau = 4, 8$, and 12 were used to perform multiscale and multifeature analysis as described in Section 3.5. Figure 4 shows the magnitude and angle responses of Gabor filters with $\tau = 8$ pixels, $l = 2.9$, and $K = 180$ as obtained for the image in Figure 1 (a). It is seen that the magnitude response is high at pixels belonging to vessels and that the angle response agrees well with the angle of the vessel at the corresponding pixel.

3.3 Line Operators

Line operators were proposed by Dixon and Taylor [24] and used by Zwiggelaar et al. [25] for the detection of linear structures in mammograms. The main line operator kernel detects horizontal lines. Assume that $N(x,y)$ is the average gray-level of M pixels along a horizontal line centered at (x,y). Next, assume that $S(x,y)$ is the average gray-level of pixels in a square of width M pixels that is horizontally aligned and centered at (x,y). The main line operator kernel is defined as $L(x,y) = N(x,y) - S(x,y)$. Detecting lines with various orientations is achieved by rotating the main kernel. Let $L_k(x,y)$ be the line opera-

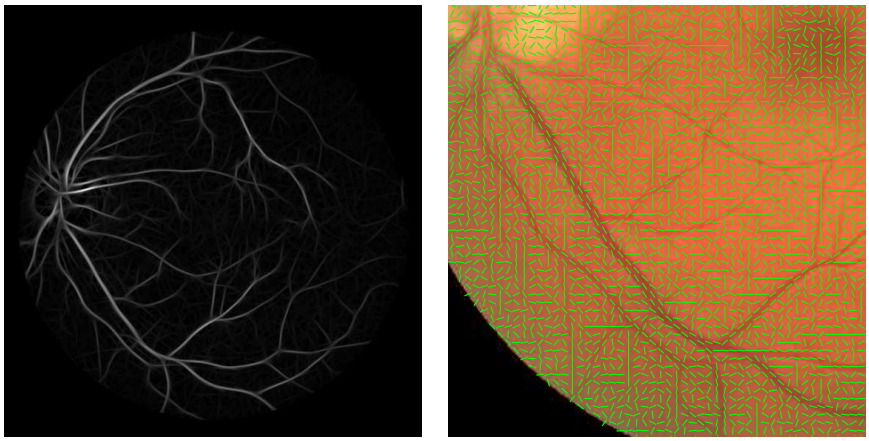

(a) (b)

Figure 4. (a) Gabor magnitude and (b) angle responses of the image in Figure 1 (a). The Gabor angle information is shown for every fifth pixel over a portion of the original color image.

tor kernel rotated to the angles $\alpha_k = -\pi/2 + \pi k/K,\ k = 0, 1, ..., K-1$. Given $W_k(x, y)$ as the result of filtering the image, $I(x, y)$, with $L_k(x, y)$, the orientation of the detected line is obtained as [22]

$$\theta(x, y) = \alpha_{k_{\max}}, \text{where } k_{\max} = \arg\{\max[W_k(x, y)]\}. \tag{10}$$

The magnitude response of the result is obtained as $W_{k_{\max}}(x, y)$. The line operator does not provide a specific parameter for scaling; multiscale analysis is performed by applying the line operator to each level of the Gaussian pyramid decomposition of the original image.

In the present work, values of $M = 15$ and $K = 180$ were determined to provide the best results for detection of vessels using the training set of the DRIVE database, and were employed for further analysis. Figure 5 shows the magnitude response of line operators as applied to the image in Figure 1 (a).

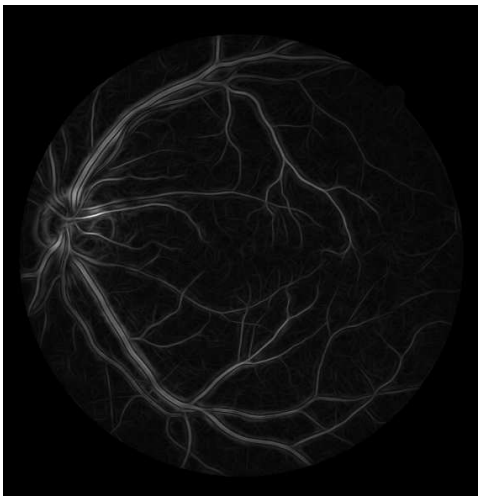

Figure 5. Magnitude response of line operators for the image in Figure 1 (a), obtained using $M = 15$ and $K = 180$.

3.4 Matched Filters

The method of Chaudhuri et al. [5], as explained in Section 1, was implemented in the present work for the detection of blood vessels. The method assumes that blood vessels have a negative contrast with respect to the background, so the Gaussian template will need to be inverted. The main kernel of the matched filter is expressed as

$$M(x, y) = -\exp\left(-x^2 / 2\sigma^2\right), \text{ for } -L/2 \leq y \leq L/2, \qquad (11)$$

where L represents the length of the vessel segment that is assumed to have a constant orientation and σ is the STD of the Gaussian. The main kernel of the filter is oriented along the y-axis; in order to detect blood vessels at different orientations, the main kernel is rotated at multiple angles.

In this work, detection of blood vessels using matched filters is performed by taking the maximum filter response of a bank of $K = 180$ filters over the range $[-\pi/2, \pi/2]$ with $L = 15$ and $\sigma = 1$, as determined

using the training set of the DRIVE database. Figure 6 represents the magnitude response of matched filters obtained for the image in Figure 1 (a).

Figure 6. Magnitude response of matched filters obtained using $L = 15$, $\sigma = 1$, and $K = 180$ for the image in Figure 1 (a).

3.5 Multifeature Analysis

In the present work, various features are combined using pattern classification methods [multilayer neural networks (MNN)] in order to distinguish pixels belonging to blood vessels from the background. The features used are:

- the vesselness measure of Frangi et al. [9],
- the vesselness measure of Salem et al. [10],
- the magnitude response of line operators [22],
- the magnitude response of matched filters [5],

- the gamma-corrected [26] inverted green component, and
- the magnitude responses of Gabor filters for $\tau = \{4, 8, 12\}$ [15].

The inverted green (G) component of the RGB color space provides high contrast for blood vessels. Therefore, a gamma-corrected version [26] of the inverted G-component image is also used as a feature in order to improve the result of classification of blood vessels. The value of gamma used for gamma correction in this work is 2.4, with the pixel values normalized to the range $[0, 1]$.

All the MNNs used in this work for multifeature analysis contain two hidden layers with 15 nodes per hidden layer. The number of input layer nodes is equal to the number of features being used and the output layer always contains one node. A tangent sigmoid (tansig) function was used as the training function for each hidden layer and a pure linear function was used at the output layer of the MNN. In each case, the MNN was trained using 10% of the available training data.

Sequential feedforward feature selection was used to determine which combination of the features listed above would provide the best results for multifeature analysis; the feature selection method selected all eight available features.

3.6 Thresholding for Segmentation of Vessels

The histogram of the intensity values of the result of vessel detection is not bimodal with a clear separation of the pixels belonging to blood vessels from the background pixels. Considering the ground-truth data provided for the 20 training images of the DRIVE database within their FOV, only 13% of an image is covered by vessel pixels. As a result, thresholding the gray-scale output images of vessel detection methods with high accuracy is a rather difficult task. Several automated thresholding methods, including Otsu's method [27], a moment-preserving thresholding method [28], the Ridler-Calvard thresholding method [31], the Rutherford-Appleton threshold selection (RATS) method [29], and an entropy-based thresholding method [30] are explored in this work. Additionally, it is possible to use a single fixed-value threshold for each

single feature or the discriminant result of multifeature analysis, obtained as the value of the point on the ROC curve that is closest to the point $[0, 1]$, with the ROC curve obtained by using the training set of images.

Considering that the majority of the pixels in a retinal image are background pixels and possess a low intensity value in the results of vessel detection methods, it could be beneficial to select a binarization threshold by analyzing only the pixels that belong to the boundaries of the vessels. We propose an adaptive thresholding method in which the boundaries of blood vessels are detected using Gabor filters with a low value of $\tau = 3$ pixels. The result is then thresholded at 0.2 of the normalized intensity to obtain the boundaries of blood vessels. Morphological dilation is then applied to the binary image of the vessel boundaries using a disk-shaped structuring element of radius two pixels to identify the adjacent regions of boundaries of blood vessels. The histogram of the pixels (with 25 bins) in the selected regions was observed to have an abrupt change in the values for two adjacent bins. The two adjacent bins with the largest probabilities of values are identified and their corresponding pixel intensity values are noted. An adaptive threshold for each image is obtained as the average of the intensity values corresponding to the two identified bins.

The performance of the proposed and selected thresholding techniques was analyzed in terms of the sensitivity (SE), specificity (SP), and accuracy (Acc) of the segmentation of blood vessels with reference to the ground-truth images provided in the DRIVE database.

3.7 Postprocessing for Removal of FP Pixels Around the ONH

In the results obtained using various vessel detection techniques, the boundary and edges of the ONH are also detected since they represent an abrupt change in intensity, i.e., an edge, which can lead to artifacts (FP pixels) when the gray-scale results are thresholded. In the present work, the FP pixels associated with the boundary of the ONH are identified using an angular difference index (ADI), defined as [1]

$$\text{ADI} = \cos\left[\theta(i,j) - \gamma(i,j)\right], \tag{12}$$

where $\theta(i,j)$ is the Gabor angle response and $\gamma(i,j)$ is the radial angle with respect to the center of the ONH, as shown in Figures 7(a) and (b), respectively. The ranges of θ and γ are limited to $[-\pi/2,\ \pi/2]$. The values of ADI are computed for each pixel within the annular region limited by two circles of radii $0.75r$ and $2r$, where $r = 0.8$ mm is the average radius of the ONH [16]. The center of the ONH was automatically detected using phase portrait analysis of the Gabor angle response [32]. The pixels for which ADI is less than 0.15, i.e., the difference between the Gabor angle and the radial angle is greater than 81°, are removed from the output of the classifier, because they represent artifacts related to the ONH. This step may cause the loss of a few pixels belonging to vessels.

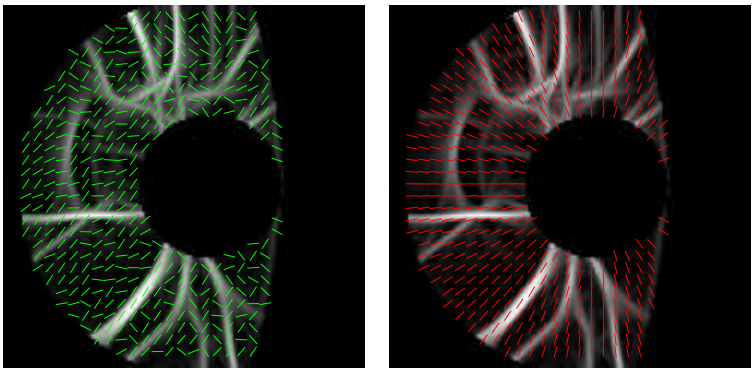

(a) (b)

Figure 7. (a) Gabor angle response and (b) radial angle with respect to the center of the ONH for the selected annular region.

4 Results

In order to obtain each feature mentioned in Section 3.5, the luminance component, Y, of the YIQ color space, defined as

$$Y = 0.299R + 0.587G + 0.114B, \tag{13}$$

where R, G, and B represent the red, green, and blue color components in the RGB color space, respectively, was used as the input to the vessel detection methods.

The performance of the proposed methods was tested with the set of 20 test images of the DRIVE database. The training set of 20 images was used to determine the best values for the parameters of the filters (Section 3), to perform the training of the MNNs (Section 3.5), and to determine a suitable threshold for segmentation of vessels (Section 3.6). The ground-truth images of blood vessels were used as reference to perform ROC analysis.

The results of detection of blood vessels were evaluated in terms of the area under the ROC curve (A_z), which are provided in Table 1. For comparative analysis, the result of another previously proposed method [6], as discussed in Section 1, that was not implemented in this work is also presented in Table 1.

Table 1. Comparison of the efficiency of detection of blood vessels in the retina obtained by different methods, as implemented in this work, and another method, for the test set (20 images) of the DRIVE database [7].

Detection method	A_z
Vesselness measure of Salem et al.	0.892
Vesselness measure of Frangi et al.	0.896
Line operators	0.905
Matched filters	0.928
Single-scale Gabor filters	0.950
Ridge-based segmentation [6]	0.952

Table 2 presents the results of performing vessel classification with MNN classifiers using various combinations of the proposed features, as mentioned in Section 3.5. For comparative analysis, the results of

the works of Soares et al. [8] and Lupaşcu et al. [13], who performed multiscale and multifeature analysis, respectively, are also presented in Table 2 (see Section 1 for the details of the methods).

Table 2. Results of detection of blood vessels in terms of A_z with the test set (20 images) of the DRIVE database. For all cases, MNN classifiers were used. Multiscale Gabor filters include the magnitude response images with scales of $\tau = \{4, 8, 12\}$ pixels. In order to keep the table entries short, the following acronyms for different features are used: Gabor filters (GF), vesselness measure of Frangi et al. (VF), vesselness measure of Salem et al. (VS), gamma-corrected green component (GC), matched filters (MF), and line operators (LO).

Detection method	A_z
VF, VS, GC, MF, and LO	0.948
Multiscale GF	0.960
Multiscale GF and LO	0.960
Multiscale GF and MF	0.960
Multiscale GF and VS	0.960
Multiscale GF and VF	0.960
Multiscale GF, VF, and GC	0.961
Multiscale GF, VF, VS, GC, MF, and LO	0.961
Multiscale complex GF [8]	0.961
Multifeature analysis (41 features) [13]	0.956

Figure 8 shows the result of multifeature and multiscale analysis for the image in Figure 1 (a) using four of the combinations given in Table 2.

Table 3 provides the performance of the three methods of entropy-based [30] thresholing, adaptive thrsholding, and fixed-value thresholding. The methods of Otsu [27], moment-preserving thresholding method [28], Ridler-Calvard thresholding method [31], and the RATS method [29] were also tested in this work; however, since they did not provide better results than the three methods mentioned above, their

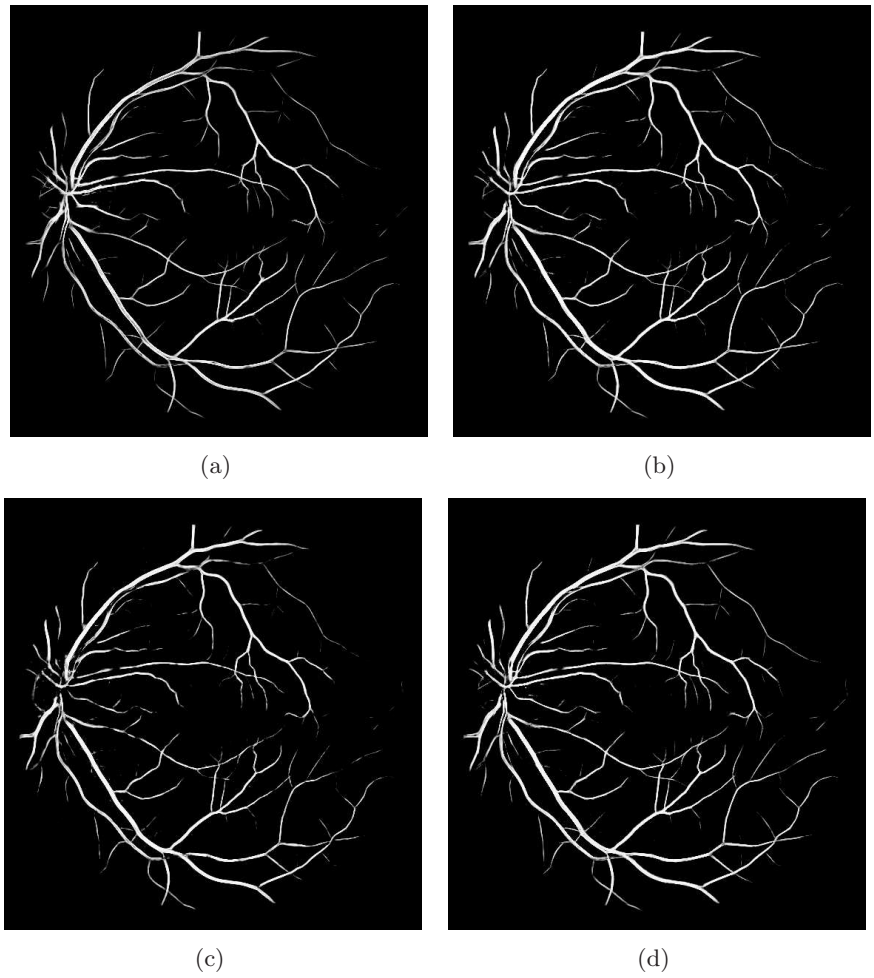

(a) (b)

(c) (d)

Figure 8. Results of multifeature and multiscale analysis using MNNs: (a) multiscale Gabor filters, (b) multiscale Gabor filters, vesselness measure of Frangi et al., and gamma-corrected inverted G-component, (c) vesselness measure of Frangi et al., vesselness measure of Salem et al., gamma-corrected inverted G-component, matched filters, and line operators, (d) multiscale Gabor filters, vesselness measure of Frangi et al., vesselness measure of Salem et al., gamma-corrected inverted G-component, matched filters, and line operators.

results are not presented in this table.

Figure 9 shows the results of thresholding the magnitude responses of single-scale Gabor filters ($\tau = 8$) [Figure 4 (a)] and the vesselness measure of Frangi et al. [Figure 3 (a)] using the fixed-value threshold, as well as the entropy-based thresholding method. It can be seen that the entropy-based method provides higher specificity [higher number of true-negative (TN) pixels] at the expense of lower sensitivity [lower number of true-positive (TP) pixels]. It can be seen that the boundary of the ONH is not segmented when using the entropy-based method in part (b) of the figure. However, the entropy-based method is incapable of segmenting the majority of the vessel pixels in the case of the vesselness measure of Frangi et al., which is likely due to the low intensity values provided by the method.

Figure 10 shows the results of thresholding the discriminant images in Figures 8 (b) and (d) obtained using multifeature analysis. Both thresholding methods perform well with the results of multifeature analysis, with the fixed-value threshold having a higher SE and the entropy-based method a higher SP. It can be seen that the boundary of the ONH is not segmented when using the entropy-based method. Note that the thresholds for parts (a) and (c) of the figure are negative, because the MNN is trained using a tansig function which maps the discriminant values to the range $[-1, 1]$.

The method for removing the FP pixels around the ONH was evaluated in combination with the methods for the detection of blood vessels based on the vesselness measures and multiscale Gabor filters. For removal of artifacts, the Gabor magnitude response image was thresholded using the fixed threshold as explained in Section 3.6, and the postprocessing technique was applied to the binarized image. The proposed postprocessing technique was applied to the 20 test images of the DRIVE database and was able to remove 224 FP pixels per image on the average, at the cost of losing 22 TP pixels per image on the average. Examples of removal of FP pixels around the ONH are shown in Figure 11.

Table 3. Performance of the proposed adaptive thresholding technique compared with the fixed-value thresholding method and the entropy-based threshold selection method. The fixed threshold was determined by using the point on the ROC curve with the shortest distance to the point $[0, 1]$ considering the 20 training images of the DRIVE database. The highest values of SE, SP, and Acc for each thresholding method are highlighted. In order to keep the table entries short, the following acronyms for different features are used: single-scale Gabor filters (SGF), multiscale Gabor filters (MGF), vesselness measure of Frangi et al. (VF), vesselness measure of Salem et al. (VS), gamma-corrected green component (GC), matched filters (MF), and line operators (LO).

	Fixed			**Entropy**			**Adaptive**		
Features	SE	SP	Acc	SE	SP	Acc	SE	SP	Acc
VS	0.816	0.886	0.877	0.056	0.998	0.875	0.863	0.752	0.766
VF	0.810	0.898	0.886	0.026	1.000	0.873	0.482	0.991	0.925
LO	0.810	0.839	0.835	0.145	0.994	0.883	0.556	0.922	0.875
MF	0.832	0.879	0.873	0.125	0.999	0.885	0.520	0.973	0.913
SGF	0.857	0.900	0.894	0.269	0.998	0.902	0.532	0.966	0.910
MGF	0.876	0.909	0.904	0.821	0.944	0.927	0.121	0.988	0.876
MGF and LO	0.876	0.912	0.907	0.827	0.945	0.929	0.150	0.974	0.867
MGF and MF	0.876	0.912	0.907	0.821	0.946	0.930	0.151	0.983	0.875
MGF and VS	0.873	0.914	0.909	0.824	0.947	0.931	0.138	0.987	0.877
MGF and VF	0.872	0.914	0.909	0.818	0.949	0.932	0.147	0.964	0.859
MGF, VF, and GC	0.877	0.914	0.909	0.829	0.948	0.932	0.134	0.993	0.882
VF, VS, GC, MF, and LO	0.853	0.903	0.896	0.806	0.944	0.926	0.128	0.990	0.878
MGF, VF, VS, GC, MF, and LO	0.876	0.918	0.912	0.856	0.934	0.924	0.146	0.983	0.874

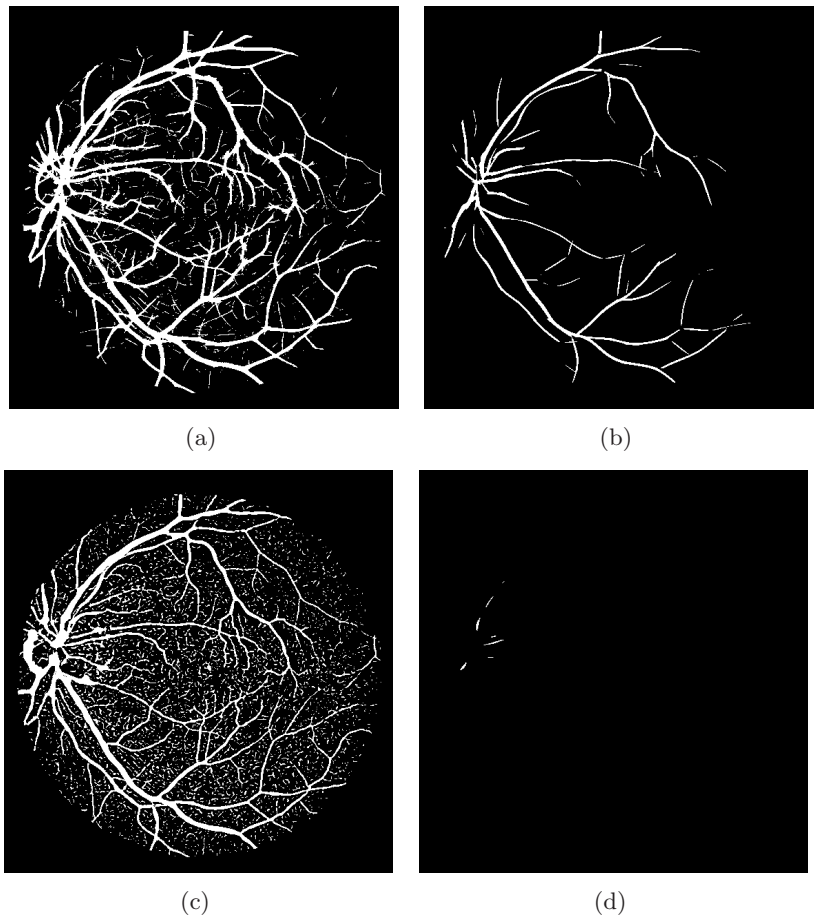

(a) (b)

(c) (d)

Figure 9. Binarized versions of the image in Figure 4 (a) (single-scale Gabor filter) using: (a) the fixed-value threshold $t = 0.0024$ of the maximum intensity value, with SE = 0.867, SP = 0.908, and Acc = 0.903; and (b) the entropy-based method ($t = 0.196$ of the normalized intensity value), with SE = 0.397, SP = 0.996, and Acc = 0.919. Binarized versions of the image in Figure 3 (a) (vesselness measure of Frangi et al.) using: (c) the fixed-value threshold $t = 3.22 \times 10^{-8}$ of the maximum intensity value, with SE = 0.810, SP = 0.889, and Acc = 0.879; and (d) the entropy-based method ($t = 0.290$ of the normalized intensity value), with SE = 0.050, SP = 1.000, and Acc = 0.871.

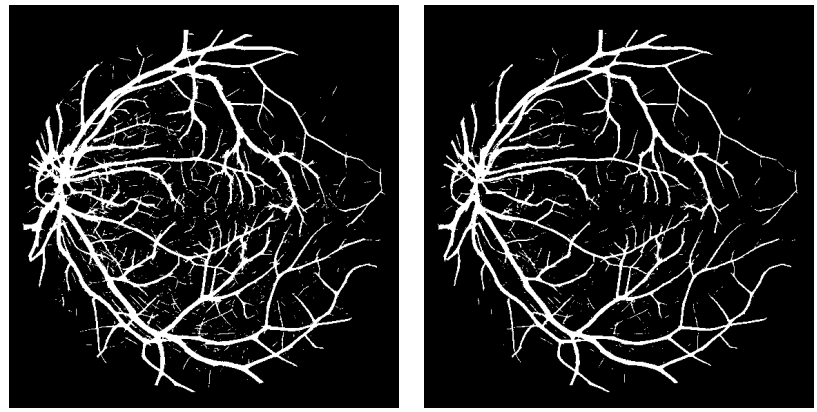

(a)

(b)

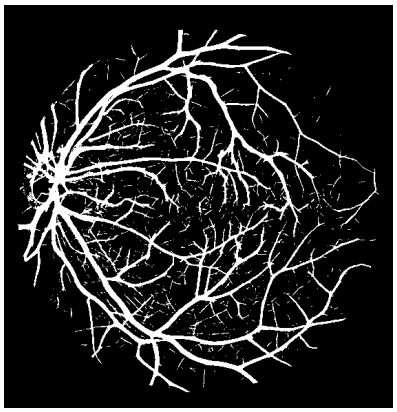

(c)

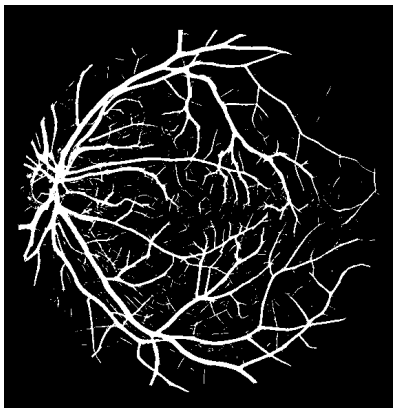

(d)

Figure 10. Binarized versions of the image in Figure 8 (b) using: (a) the fixed-value threshold $t = -0.743$ of the maximum intensity value, with SE = 0.893, SP = 0.909, and Acc = 0.907; and (b) the entropy-based method ($t = 0.263$ of the normalized intensity value), with SE = 0.837, SP = 0.950, and Acc = 0.936. Binarized versions of the image in Figure 8 (d) using: (c) the fixed-value threshold $t = -0.740$ of the maximum intensity value, with SE = 0.895, SP = 0.909, and Acc = 0.908; and (d) the entropy-based method ($t = 0.302$ of the normalized intensity value), with SE = 0.870, SP = 0.933, and Acc = 0.925.

(a) (b)

Figure 11. Example of removal of ONH artifacts: (a) thresholded Gabor magnitude response image, and (b) the same region after the removal of ONH artifacts.

5 Discussion

As evident from the results in Table 1, even the use of a combination of large number of features (41) [13], does not lead to substantial increase in the value of A_z. The large number of FP pixels caused by over segmentation of small blood vessels seems to be the limiting factor in achieving higher A_z values. The accuracy of detection of blood vessels could be increased if thin, single-pixel-wide blood vessels are detected accurately. However, thin blood vessels may not be important in the analysis of retinal vasculature as only changes in the major vessels have been observed to be clinically significant [23, 33].

Based on the results obtained in this work, a single-scale Gabor filter is capable of detecting blood vessels with accuracy ($A_z = 0.950$) not substantially different from the highest A_z value obtained with the result of multifeature analysis in this work ($A_z = 0.961$). It would be of interest to determine if the difference between the A_z values given above is statistically significant.

Using a Lenovo Thinkpad T510, equipped with an Intel Core i7

(Hyper-threaded-dual-core) 2.67-GHz processor, 4 MB of level 2 cache, 8 GB of DDR3 RAM, running 64-bit Windows 7 Professional, and using 64-bit Matlab software, the run time for single-scale Gabor filters with $K = 180$, for a single color image from the DRIVE database is approximately 13.5 seconds. The preprocessing step takes about 8.8 seconds to execute.

Although the reduction of FP pixels is visible in the example shown in Figure 11, the result did not lead to a substantial increase in specificity. This is mainly because the total number of FP pixels removed (224 pixels, on the average, per image) by the postprocessing step is small compared to the total number of FP pixels (20, 038 pixels, on the average, per image) and the total number of TP pixels (24, 888 pixels, on the average, per image). Such a postprocessing step is most beneficial when applied to a skeleton of the vasculature in applications where it is important to process only pixels that belong to vessels, such as tracking the major branches of vessels [34] and measurement of vessel thickness [35].

The problem of segmentation of vessels via thresholding is crucial to applications that deal with measurement and analysis of the statistics of blood vessels. In this work, we have analyzed seven different thresholding methods. Based on the results presented in Table 3, the thresholding method using a fixed value obtained using the ROC curve for the training set of images provides the most consistent results in terms of SE, SP, and accuracy. The entropy-based thresholding method provides a higher SP and similar SE in comparison to the fixed-value method when applied to the results of multifeature analysis. However, the entropy-based method has low sensitivity when applied to single features. The proposed adaptive thresholding method does not perform better than the other two methods. Depending on the desired application, either the fixed-value method, the entropy-based method, or a combination of the two could be employed.

6 Conclusion

In this study, we have analyzed multiscale and multifeature methods for the detection of blood vessels in retinal fundus images, and achieved a maximum A_z value of 0.961 using the 20 test images of the DRIVE database. The results of the present study indicate that the state-of-the-art methods for the detection of blood vessels perform at high levels of efficiency and that combining several features may not yield better results. The result of the fixed-value thresholding or the entropy-based method could be helpful in analyzing the thickness and tortuosity of blood vessels.

References

[1] A. K. Dhara, R. M. Rangayyan, F. Oloumi, S. Mukhopadhyay. "Methods for the detection of blood vessels in retinal fundus images and reduction of false-positive pixels around the optic nerve head," in *Proc. 4th IEEE International Conference on E-Health and Bioengineering - EHB 2013*, Iaşi, Romania, November 2013, pp. 1–6.

[2] N. Patton, T. M. Aslam, T. MacGillivray, I. J. Deary, B. Dhillon, R. H. Eikelboom, K. Yogesan, I. J. Constable. "Retinal image analysis: Concepts, applications and potential," *Progress in Retinal and Eye Research*, vol. 25, no. 1, pp. 99–127, 2006.

[3] American Academy of Pediatrics, American Association for Pediatric Ophthalmology and Strabismus, American Academy of Ophthalmology, "Screening examination of premature infants for retinopathy of prematurity," *Pediatrics*, vol. 108, pp. 809–811, 2001.

[4] R. van Leeuwen, U. Chakravarthy, J. R. Vingerling, C. Brussee, A. Hooghart, P. Mudler, P. de Jong. "Grading of age-related maculopathy for epidemiological studies: Is digital imaging as good as 35-mm film?," *Ophthalmology*, vol. 110, no. 8, pp. 1540–1544, 2003.

[5] S. Chaudhuri, S. Chatterjee, N. Katz, M. Nelson, M. Goldbaum. "Detection of blood vessels in retinal images using two-dimensional matched filters," *IEEE Transactions on Medical Imaging*, vol. 8, no. 3, pp. 263–269, 1989.

[6] J. Staal, M. D. Abràmoff, M. Niemeijer, M. A. Viergever, B. van Ginneken. "Ridge-based vessel segmentation in color images of the retina," *IEEE Transactions on Medical Imaging*, vol. 23, no. 4, pp. 501–509, 2004.

[7] "DRIVE: Digital Retinal Images for Vessel Extraction," www. isi.uu.nl/ Research/ Databases/ DRIVE/ , accessed December 2013.

[8] J. V. B. Soares, J. J. G. Leandro, R. M. Cesar Jr., H. F. Jelinek, M. J. Cree. "Retinal vessel segmentation using the 2-D Gabor wavelet and supervised classification," *IEEE Transactions on Medical Imaging*, vol. 25, no. 9, pp. 1214–1222, 2006.

[9] A. F. Frangi, W. J. Niessen, K. L. Vincken, M. A. Viergever. "Multiscale vessel enhancement filtering," in *Medical Image Computing and Computer-Assisted Intervention - MICCAI98*, vol. 1496 of *Lecture Notes in Computer Science*, pp. 130–137. Springer, Berlin, Germany, 1998.

[10] M. N. Salem, A. S. Salem, A. K. Nandi. "Segmentation of retinal blood vessels based on analysis of the Hessian matrix and clustering algorithm," in *15th European Signal Processing Conference (EUSIPCO 2007)*, Poznan, Poland, September 2007, pp. 428–432.

[11] C.-H. Wu, G. Agam, P. Stanchev. "A hybrid filtering approach to retinal vessel segmentation," in *Biomedical Imaging: From Nano to Macro, 4th IEEE International Symposium on*, Arlington, VA, April 2007, pp. 604–607.

[12] "Structured Analysis of the Retina," http:// www. parl. clemson. edu/ ahoover/ stare/ index. html, accessed December 2013.

[13] C. A. Lupaşcu, D. Tegolo, E. Trucco. "FABC: Retinal vessel segmentation using AdaBoost," *IEEE Transactions on Information Technology in Biomedicine*, vol. 14, no. 5, pp. 1267–1274, September 2010.

[14] M. Sofka, C. V. Stewart. "Retinal vessel centerline extraction using multiscale matched filters, confidence and edge measures," *IEEE Transactions on Medical Imaging*, vol. 25, no. 12, pp. 1531–1546, December 2006.

[15] R. M. Rangayyan, F. J. Ayres, Faraz Oloumi, Foad Oloumi, P. Eshghzadeh-Zanjani. "Detection of blood vessels in the retina with multiscale Gabor filters," *Journal of Electronic Imaging*, vol. 17, pp. 023018:1–7, April-June 2008.

[16] F. Oloumi, R. M. Rangayyan, A. L. Ells. *Digital Image Processing for Ophthalmology: Detection and Modeling of the Retinal Vascular Architecture*, Morgan & Claypool, 2014, In press.

[17] T. Lindeberg. "Edge detection and ridge detection with automatic scale selection," *International Journal of Computer Vision*, vol. 30, no. 2, pp. 117–154, 1998.

[18] B. S. Y. Lam, Y. Gao, A.W.-C. Liew. "General retinal vessel segmentation using regularization-based multiconcavity modeling," *IEEE Transactions on Medical Imaging*, vol. 29, no. 7, pp. 1369–1381, July 2010.

[19] T. Stŏsić, B. D. Stŏsić. "Multifractal analysis of human retinal vessels," *IEEE Transactions on Medical Imaging*, vol. 25, no. 8, pp. 1101–1107, 2006.

[20] F. Zana, J. C. Klein. "Segmentation of vessel-like patterns using mathematical morphology and curvature estimation," *IEEE Transactions on Image Processing*, vol. 10, no. 7, pp. 1010–1019, July 2001.

[21] M. Foracchia, E. Grisan, A. Ruggeri. "Detection of optic disc in retinal images by means of a geometrical model of vessel structure," *IEEE Transactions on Medical Imaging*, vol. 23, no. 10, pp. 1189–1195, 2004.

[22] F. J. Ayres, R. M. Rangayyan. "Design and performance analysis of oriented feature detectors," *Journal of Electronic Imaging*, vol. 16, no. 2, pp. 023007:1–12, 2007.

[23] C. M. Wilson, K. D. Cocker, M. J. Moseley, C. Paterson, S. T. Clay, W. E. Schulenburg, M. D. Mills, A. L. Ells, K. H. Parker, G. E. Quinn, A. R. Fielder, J. Ng. "Computerized analysis of retinal vessel width and tortuosity in premature infants," *Investigative Ophthalmology and Visual Science*, vol. 49, no. 1, pp. 3577–3585, 2008.

[24] R. N. Dixon, C. J. Taylor. "Automated asbestos fibre counting," in *Institute of Physics Conference Series*, 1979, vol. 44, pp. 178–185.

[25] R. Zwiggelaar, S. M. Astley, C. R. M. Boggis, C. J. Taylor. "Linear structures in mammographic images: detection and classification," *IEEE Transactions on Medical Imaging*, vol. 23, no. 9, pp. 1077–1086, 2004.

[26] R. C. Gonzalez, R. E. Woods. *Digital Image Processing*, Prentice Hall, Upper Saddle River, NJ, 2nd edition, 2002.

[27] N. Otsu. "A threshold selection method from gray-level histograms," *IEEE Transactions on Systems, Man, and Cybernetics*, vol. SMC-9, pp. 62–66, 1979.

[28] W.-H. Tsai. "Moment-preserving thresholding: A new approach," *Computer Vision, Graphics, and Image Processing*, vol. 29, no. 3, pp. 377–393, 1985.

[29] J. Kittler, J. Illingworth, J. Föglein. "Threshold selection based on a simple image statistic," *Computer Vision, Graphics, and Image Processing*, vol. 30, pp. 125–147, 1985.

[30] J. N. Kapur, P. K. Sahoo, A. K. C. Wong. "A new method for gray-level picture thresholding using the entropy of the histogram," *Computer Vision, Graphics, and Image Processing*, vol. 29, pp. 273–285, 1985.

[31] T. W. Ridler, S. Calvard. "Picture thresholding using an iterative selection method," *IEEE Transactions on Systems, Man, and Cybernetics*, vol. 8, pp. 630–632, Aug 1978.

[32] R. M. Rangayyan, X. Zhu, F. J. Ayres, A. L. Ells. "Detection of the optic nerve head in fundus images of the retina with Gabor filters and phase portrait analysis," *Journal of Digital Imaging*, vol. 23, no. 4, pp. 438–453, August 2010.

[33] C. M. Wilson, K. Wong, J. Ng, K. D. Cocker, A. L. Ells, A. R. Fielder. "Digital image analysis in retinopathy of prematurity: A comparison of vessel selection methods," *Journal of American Association for Pediatric Ophthalmology and Strabismus*, vol. 16, no. 3, pp. 223 – 228, 2011.

[34] F. Oloumi, R. M. Rangayyan, A. L. Ells. "Tracking the major temporal arcade in retinal fundus images," in *Proc. IEEE Canada 27th Annual Canadian Conference on Electrical and Computer Engineering (CCECE)*, Toronto, ON, Canada, May 2014.

[35] F. Oloumi, R. M. Rangayyan, A. L. Ells. "Measurement of vessel width in retinal fundus images of preterm infants with plus disease," in *Proc. IEEE International Symposium on Medical Measurements and Applications (MeMeA)*, Lisbon, Portugal, May 2014, In press.

[36] "Hessian based Frangi vesselness filter," http:// www. mathworks. com/ matlabcentral/ fileexchange/ 24409- hessian- based- frangi-vesselness- filter.

Faraz Oloumi, Ashis K. Dhara,
Rangaraj M. Rangayyan, and Sudipta Mukhopadhyay

Received June 5, 2014

Faraz Oloumi and Rangaraj M. Rangayyan*
Department of Electrical and Computer Engineering,
Schulich School of Engineering, University of Calgary,
Calgary, Alberta, Canada T2N 1N4.
Phone: +1 (403) 220 − 6745
E–mail: *ranga@ucalgary.ca

Ashis K. Dhara and Sudipta Mukhopadhyay
Department of Electronics and Electrical Communication Engineering,
Indian Institute of Technology,
Kharagpur 721302, India
Phone: +91 3222 283568